Available online at www.sciencedirect.com
SCIENCE DIRECT®
PERGAMON
International Journal of Heat and Mass Transfer 46 (2003) 2927–2946
International Journal of HEAT and MASS TRANSFER
www.elsevier.com/locate/ijhmt

Forced and mixed convective heat transfer from accelerated flow past an elliptic cylinder

S.J.D. D'Alessio *, M.G. Saunders, D.L. Harmsworth

Department of Applied Mathematics, University of Waterloo, Waterloo, Ont., Canada N2L 3G1

Received 25 June 2002; received in revised form 4 February 2003

Abstract

Investigated in this paper are the initial stages of the laminar, two-dimensional, thermal-fluid problem of forced and mixed convective heat transfer from accelerated flow past an elliptic cylinder. The cylinder is taken to be inclined at an angle η with the horizontal and the viscous incompressible Boussinesq fluid accelerates uniformly from rest past it. Two types of solutions are presented. The first type takes the form of an approximate analytical solution valid for small times and large Reynolds numbers. The second type is a numerical solution obtained by numerically integrating the full Navier–Stokes and energy equations using a spectral-finite difference procedure.

1. Introduction

In this paper we investigate forced and mixed convective heat transfer from an inclined elliptic cylinder. The cylinder is inclined at an angle η with the horizontal, and starting from rest, accelerates uniformly through a viscous incompressible fluid. The fluid motion remains two-dimensional and laminar for all time and the cylinder motion is perpendicular to the gravitational acceleration. Also, the temperature of the cylinder surface is constant and is taken to be higher than that of the surrounding fluid. The flow configuration is illustrated in Fig. 1. As shown in Fig. 1, a frame of reference that translates with the cylinder has been employed so as to simplify the boundary conditions on the surface. In this frame the cylinder is stationary while the fluid accelerates past it; this is the problem that we will solve. The emphasis here is on the initial development of the flow and of the heat transfer process. Although the problem described is idealized and highly simplified, it is nonetheless general enough to encompass all elliptical cross sections between the limiting cases of a circular cylinder and a flat plate. Also, it is a reasonable prototypical model for simulating the thermal-fluid start-up of a cylindrical body from rest, and for studying important aspects of unsteady flow separation. One purpose of the present study is to reconcile numerical solutions of the Navier–Stokes and energy equations with an analytic solution which is valid for small times following the start of the motion and for large Reynolds numbers, R. In addition, this study also serves as a good approximation for other more complicated initial flows. For example, the oscillating flow having the far-field velocity given by $U(t) = U_0 \sin(\gamma t)$ is well approximated by $U(t) \sim U_0 \gamma t$ for small times. Hence, its initial flow structure should mirror that presented in this work (with $b = U_0\gamma$).

Other studies regarding accelerating flows past cylindrical bodies include: Collins and Dennis [1], Badr et al. [2] and more recently D'Alessio and Chapman [3]. The work by Collins and Dennis considers symmetrical flow past a uniformly accelerating circular cylinder while the paper by Badr et al. considers a circular cylinder moving with speed varying according to $U(t) = U_0 + U_1 t + U_2 t^2$. The work by D'Alessio and Chapman addresses uniformly accelerating motion past an inclined elliptic cylinder. The present study represents an extension of that problem to incorporate heat transfer effects. Concerning uniform flows past elliptic cylinders, recent

* Corresponding author. Fax: +1-519-746-0274.
E-mail address: sdalessio@math.uwaterloo.ca (S.J.D. D'Alessio).

0017-9310/03/$ - see front matter
doi:10.1016/S0017-9310(03)00090-5

Nomenclature

a_1, a_2, a_3	numerical constants
A, B, A_0, B_0, A_1, B_1	functions defined by Eqs. (9), (10), (25), (36)
b	uniform rate of acceleration
c	semi-focal length
C_D	drag coefficient
C_L	lift coefficient
E_1, E_2	functions used in Eq. (49)
f_n, F_n	Fourier coefficients for the stream function
g	gravitational acceleration
$\vec{g}$	gravitational vector
G	scalar potential function
H, h	arbitrary functions used in Eqs. (28), (68)
K	function defined by Eq. (49)
M	metric of transformation
M_0	metric of transformation evaluated on the cylinder surface
n, m	cylinder semi-minor, semi-major axes respectively
$N \times L$	used to denote the grid size
N_f	number of terms retained in Fourier series
Nu	local Nusselt number
$\overline{Nu}$	average Nusselt number
p	arbitrary function used in Eq. (68)
P	pressure
P^*	scaled pressure
Pr	Prandtl number, ν/κ
q	function representing right-hand side
r	aspect ratio, n/m
r_n, s_n	Fourier coefficients for the vorticity
R	Reynolds number, $2c\sqrt{cb}/\nu$
Ra	Rayleigh number, $\alpha g(T_0 - T_\infty)/b$
s	scaled coordinate, $s = M_0 z$
t	time
T	dimensional temperature
x, y	Cartesian coordinates
X, Y	drag and lift forces along major and minor axis
u, v	velocity components
$\vec{V}$	velocity vector
$\vec{W}$	vorticity vector
z	scaled coordinate
z_∞	outer boundary location used in numerical scheme

Greek symbols

α	thermal expansion coefficient
β	computational parameter, $n\lambda$
$\delta_{1,n}$	Kronecker delta
Δt	time increment in numerical scheme
κ	thermal diffusivity
ν	kinematic viscosity
ξ, θ	elliptic coordinates
ξ_0	constant defined by Eq. (4)
η	angle of inclination
λ	scaling parameter, $\sqrt{8t/R}$
ϕ	dimensionless temperature, $(T - T_\infty)/(T_0 - T_\infty)$
Φ	scaled dimensionless temperature
ψ	stream function
Ψ	scaled stream function
ζ	vorticity
ω	scaled vorticity
χ	generic flow variable

Subscripts

0	surface value or leading order terms
∞	value at infinity
ij	terms in the series (34)

Superscript

$*$	dimensional quantity

studies include Patel [4], Shintani et al. [5], D'Alessio [6], Nair and Sengupta [7], and Badr et al. [8].

In the literature there are numerous heat transfer studies involving cylinders and forced, free or mixed convection. Here, we will highlight only some of the more recent mixed convection papers. For the circular geometry these include the investigations by Badr [9], Bassam and Abu-Hijleh [10,11] and Badr and Mahfouz [12]. These are all numerical studies where the far-field flow is either uniform or fluctuating periodically about a uniform background flow. Nguyen et al. [13], on the other hand, consider mixed convection from a rotating circular cylinder undergoing small fluctuations in the free-stream velocity. For the elliptic geometry there is a recent numerical study by Ahmad and Badr [14] involving mixed convection in a fluctuating free stream and a work by Nishiyama et al. [15] dealing with elliptic cylinders in a tandem arrangement, to mention just two. To our knowledge there are no prior studies devoted to heat transfer from accelerating flows past elliptic cylinders. This work attempts to introduce the problem and offers both numerical and analytical solutions to the initial flow and heat transfer process.

The paper is structured as follows. Presented in the next section are the governing equations, with their corresponding initial and boundary conditions. A convenient coordinate system for the elliptic geometry is also introduced. The analytical solution procedure is then discussed in Section 3. This first involves casting the equations in boundary-layer coordinates which incor-

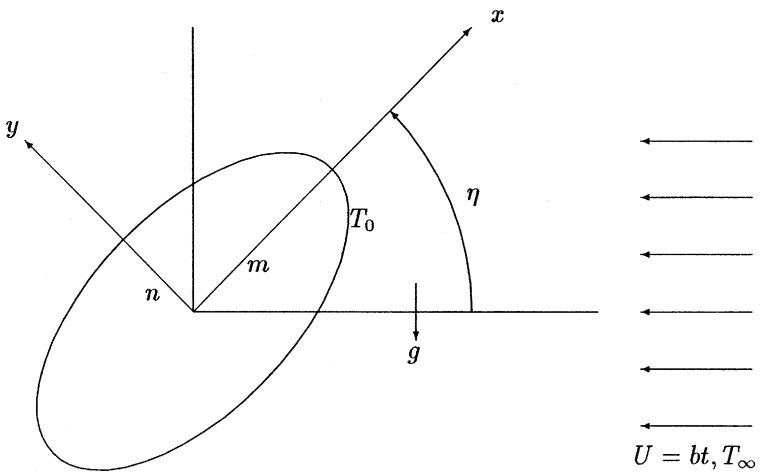

Fig. 1. Flow set up.

porate the parameter $\lambda = \sqrt{8t/R}$ and then expanding the flow variables in a double series. In Section 4 a numerical method for solving the governing equations is provided. The technique employed is a spectral—finite difference scheme specifically designed to capture the early stages of the flow. Following this is the "Results and comparisons" Section 5. There, the numerical solution is compared with the analytical solution using derived quantities such as the drag, lift and heat transfer coefficients. Lastly, the paper is summarized in Section 6.

2. Governing equations and boundary conditions

The problem under consideration is assumed to be two-dimensional, and therefore it is worth expressing the governing Navier–Stokes equations in terms of a stream function ψ and scalar vorticity ζ. The dimensionless functions ψ and ζ are related to their dimensional counterparts ψ^* and ζ^* through the scaling

$$\psi^* = c\sqrt{cb}\psi, \quad \zeta^* = \sqrt{cb}\zeta/c, \tag{1}$$

where $2c$ is the focal length of the ellipse and $c = \sqrt{m^2 - n^2}$ with m and n denoting the semi-major and semi-minor axis lengths respectively. Here, b refers to the uniform rate of acceleration of the oncoming flow. The dimensionless velocity components u, v are obtained by dividing the corresponding dimensional components u^*, v^* by $\sqrt{cb}$. The dimensional temperature T is rendered dimensionless through

$$\phi = \frac{T - T_\infty}{T_0 - T_\infty}, \tag{2}$$

with ϕ denoting the dimensionless temperature, and T_0, T_∞ denoting the constant surface and far-field temperatures respectively (and $T_0 > T_\infty$). The temperature difference $T_0 - T_\infty$ gives rise to the buoyancy force which will also induce fluid motion.

The Cartesian coordinate system is not convenient for either analytical or numerical purposes. Instead, we introduce a conformal transformation which generates a coordinate system that is better suited to the geometry of the problem:

$$x + iy = \cosh[(\xi + \xi_0) + i\theta]. \tag{3}$$

This transformation maps the surface of the cylinder to $\xi = 0$ and the infinite region exterior to the cylinder to the semi-infinite rectangular strip $\xi \geqslant 0$, $0 \leqslant \theta \leqslant 2\pi$. The constant ξ_0 appearing in (3) is defined by

$$\tanh \xi_0 = r, \tag{4}$$

where $r = n/m$ is the ratio of the minor to major axes of the ellipse. In the transformed coordinates (ξ, θ) the equations dictating the fluid motion are:

$$\frac{\partial^2\psi}{\partial\xi^2} + \frac{\partial^2\psi}{\partial\theta^2} = M^2\zeta, \tag{5}$$

$$\frac{\partial\zeta}{\partial t} = \frac{1}{M^2}\left[-\frac{\partial\psi}{\partial\xi}\frac{\partial\zeta}{\partial\theta} + \frac{\partial\psi}{\partial\theta}\frac{\partial\zeta}{\partial\xi} + \frac{2}{R}\left(\frac{\partial^2\zeta}{\partial\xi^2} + \frac{\partial^2\zeta}{\partial\theta^2}\right) + Ra\left(A\frac{\partial\phi}{\partial\xi} - B\frac{\partial\phi}{\partial\theta}\right)\right], \tag{6}$$

$$\frac{\partial\phi}{\partial t} = \frac{1}{M^2}\left[-\frac{\partial\psi}{\partial\xi}\frac{\partial\phi}{\partial\theta} + \frac{\partial\psi}{\partial\theta}\frac{\partial\phi}{\partial\xi} + \frac{2}{RPr}\left(\frac{\partial^2\phi}{\partial\xi^2} + \frac{\partial^2\phi}{\partial\theta^2}\right)\right], \tag{7}$$

where M refers to the metric of the transformation given by

$$M^2(\xi, \theta) = \frac{1}{2}[\cosh 2(\xi + \xi_0) - \cos(2\theta)] \tag{8}$$

and the functions A, B are defined by

$$A(\xi,\theta) = \sinh(\xi+\xi_0)\cos\eta\cos\theta - \cosh(\xi+\xi_0) \times \sin\eta\sin\theta, \tag{9}$$

$$B(\xi,\theta) = \cosh(\xi+\xi_0)\cos\eta\sin\theta + \sinh(\xi+\xi_0) \times \sin\eta\cos\theta. \tag{10}$$

The velocity components (v_ξ, v_θ) in the directions of (ξ,θ) become

$$v_\xi = -\frac{1}{M}\frac{\partial\psi}{\partial\theta}, \quad v_\theta = \frac{1}{M}\frac{\partial\psi}{\partial\xi} \tag{11}$$

and the vorticity is found through

$$\zeta = \frac{1}{M^2}\left[-\frac{\partial}{\partial\theta}(Mv_\xi) + \frac{\partial}{\partial\xi}(Mv_\theta)\right]. \tag{12}$$

In the above system, the dimensionless time t is related to the dimensional time t^* through $t = \sqrt{b}t^*/\sqrt{c}$ and the familiar dimensionless parameters appearing in the equations include:

$$R = \frac{2c\sqrt{cb}}{\nu}, \quad Ra = \frac{\alpha g(T_0 - T_\infty)}{b}, \quad Pr = \frac{\nu}{\kappa} \tag{13}$$

and denote the Reynolds, Rayleigh and Prandtl numbers respectively. Here, ν refers to the kinematic viscosity, g the acceleration due to gravity, α the thermal expansion coefficient of the fluid, and κ refers to the thermal diffusivity of the fluid. We point out that implicit in Eqs. (5)–(7) are the simplifications that all the fluid properties, with the exception of density, are taken to be constant in the temperature range $T_0 < T < T_\infty$, viscous dissipation and radiative effects are neglected, and the buoyancy force is prescribed using the Boussinesq approximation. Also, the effects due to heat conduction in the cylinder interior are ignored.

Surface boundary conditions corresponding to ψ, ζ and ϕ include the no-slip, impermeable and isothermal conditions

$$\psi = 0, \quad \frac{\partial\psi}{\partial\xi} = 0 \text{ and } \phi = 1 \text{ on } \xi = 0. \tag{14}$$

We also invoke the periodicity conditions given by

$$\begin{aligned}\psi(\xi,\theta,t) &= \psi(\xi,\theta+2\pi,t),\\ \zeta(\xi,\theta,t) &= \zeta(\xi,\theta+2\pi,t),\\ \phi(\xi,\theta,t) &= \phi(\xi,\theta+2\pi,t).\end{aligned} \tag{15}$$

Next, the far-field conditions to be enforced are

$$\mathrm{e}^{-\xi}\frac{\partial\psi}{\partial\xi} \to \frac{1}{2}t\mathrm{e}^{\xi_0}\sin(\theta+\eta), \quad \mathrm{e}^{-\xi}\frac{\partial\psi}{\partial\theta} \to \frac{1}{2}t\mathrm{e}^{\xi_0}\cos(\theta+\eta),$$
$$\zeta,\phi \to 0 \text{ as } \xi\to\infty. \tag{16}$$

The above conditions correspond to a far-field fluid velocity that increases linearly with time (in accordance with the uniform rate of acceleration), and as such the far-field vorticity vanishes, as does the scaled temperature. By inspecting the boundary conditions we see that there are two surface conditions for the stream function, but none for the vorticity. A method of determining the surface vorticity involves the use of integral conditions. These global conditions are given by

$$\begin{aligned}&\frac{1}{\pi}\int_0^\infty\int_0^{2\pi}\mathrm{e}^{-n\xi}M^2\zeta\sin(n\theta)\,\mathrm{d}\theta\,\mathrm{d}\xi = t\mathrm{e}^{\xi_0}\cos(\eta)\delta_{1,n},\\ &\quad n = 1,2,\ldots,\\ &\frac{1}{\pi}\int_0^\infty\int_0^{2\pi}\mathrm{e}^{-n\xi}M^2\zeta\cos(n\theta)\,\mathrm{d}\theta\,\mathrm{d}\xi = t\mathrm{e}^{\xi_0}\sin(\eta)\delta_{1,n},\\ &\quad n = 0,1,\ldots,\end{aligned} \tag{17}$$

where $\delta_{1,n}$ is the Kronecker delta defined as

$$\delta_{1,n} = \begin{cases}1 & \text{if } n = 1,\\ 0 & \text{if } n \neq 1.\end{cases} \tag{18}$$

Basically, we have converted the boundary conditions on the surface and at large distances into conditions that are valid throughout the entire domain. This was accomplished by using Green's second identity, the details of which are contained in Dennis and Quartapelle [16]. Later, we will explain how these integral conditions can be used in determining the surface vorticity.

Lastly, we specify the initial conditions. Since the fluid motion starts from rest, the initial conditions for ψ and ζ are simply

$$\psi(\xi,\theta,t=0) = \zeta(\xi,\theta,t=0) = 0. \tag{19}$$

The initial temperature distribution, on the other hand, will be given by

$$\phi(\xi,\theta,t=0) = \begin{cases}1 & \text{on } \xi = 0,\\ 0 & \text{for } \xi \neq 0.\end{cases} \tag{20}$$

It is clear that this initial distribution is singular; this will have consequences on the initial heat transfer process and will be addressed in the following sections.

3. Analytical solution procedure

There are several well known analytical techniques available for deriving approximate solutions for the early development of the flow and heat transfer process. For example, the methods of successive approximation, multiple series expansion and matched asymptotic expansions are all appropriate choices for this problem. We have decided to utilize the multiple series expansion method taking advantage of the fact that it leads to a set of what are effectively linear ordinary differential equations, exhibiting an obvious pattern.

To help the reader appreciate the details of the multiple series expansion, it is worth mentioning how the leading order terms ψ_0, ζ_0 and ϕ_0 can be reasoned. By examining Eqs. (5)–(7) and making the usual boundary-layer type approximations, these equations simplify to

$$\frac{\partial^2\psi_0}{\partial\xi^2} = M_0^2\zeta_0, \tag{21}$$

$$\frac{\partial\zeta_0}{\partial t} = \frac{1}{M_0^2}\left[\frac{2}{R}\frac{\partial^2\zeta_0}{\partial\xi^2} + RaA_0\frac{\partial\phi_0}{\partial\xi}\right], \tag{22}$$

$$\frac{\partial\phi_0}{\partial t} = \frac{2}{M_0^2 RPr}\frac{\partial^2\phi_0}{\partial\xi^2}, \tag{23}$$

where

$$M_0^2(\theta) = M^2(\xi=0,\theta) = \frac{1}{2}[\cosh(2\xi_0) - \cos(2\theta)], \tag{24}$$

$$\begin{aligned} A_0(\theta) &= A(\xi=0,\theta) \\ &= \sinh\xi_0\cos\eta\cos\theta - \cosh\xi_0\sin\eta\sin\theta. \end{aligned} \tag{25}$$

The solution to this system of coupled partial differential equations can be found by first solving the heat equation (23). The similarity solution satisfying the boundary conditions (14) and (16) is easily found to be

$$\phi_0(\xi,\theta,t) = 1 - \operatorname{erf}\left(\frac{\sqrt{Pr}M_0\xi}{\sqrt{8t/R}}\right) = \operatorname{erfc}\left(\frac{\sqrt{Pr}M_0\xi}{\sqrt{8t/R}}\right), \tag{26}$$

where

$$\operatorname{erf}(x) = \frac{2}{\sqrt{\pi}}\int_0^x \mathrm{e}^{-u^2}\,\mathrm{d}u, \tag{27}$$

is the error function. Substituting this solution into Eq. (22) yields another heat equation, this time with a source term. The particular solution corresponding to the source term will have a relatively simple form when $Pr = 1$. For this reason we set $Pr = 1$ and arrive at the following similarity solution:

$$\begin{aligned} \zeta_0(\xi,\theta,t) = {} & \frac{t}{\sqrt{8t/R}}\left[\frac{1}{\sqrt{\pi}M_0}\exp\left(\frac{-M_0^2\xi^2}{8t/R}\right)\right. \\ & \left. - \frac{\xi}{\sqrt{8t/R}}\operatorname{erfc}\left(\frac{M_0\xi}{\sqrt{8t/R}}\right)\right]H(\theta) \\ & + \frac{2RaA_0t}{\sqrt{8t/R}}\left[\frac{1}{\sqrt{\pi}M_0}\exp\left(\frac{-M_0^2\xi^2}{8t/R}\right)\right. \\ & \left. - \frac{2\xi}{\sqrt{8t/R}}\operatorname{erfc}\left(\frac{M_0\xi}{\sqrt{8t/R}}\right)\right], \end{aligned} \tag{28}$$

where $H(\theta)$ is an arbitrary function which can be determined by imposing the integral conditions (17). Lastly, the stream function ψ_0 can then easily be found by substituting (28) into Eq. (21) and applying the boundary conditions (14). These details will not be presented since the relevant scaling information is already present in the solutions given by (26) and (28).

The procedure just outlined represents the first stage in the method of successive approximation. The similarity solutions obtained suggest that we consider the similarity variable z defined by

$$z = \frac{\xi}{\lambda} \quad \text{where } \lambda = \sqrt{\frac{8t}{R}}. \tag{29}$$

The spatial coordinate z can be referred to as a boundary-layer coordinate. The parameter λ describes the diffusive growth of the evolving boundary layer. An advantage of working in terms of the boundary-layer coordinate z is that the physical coordinate ξ becomes a moving coordinate; that is, lines of constant z expand in time when plotted in a Cartesian coordinate system. This is ideal from a numerical point of view, since the grid lines are allowed to expand with the growing boundary layer to ensure adequate resolution during the early stages of the flow.

We now formally discuss the multiple series expansion method. We begin by making the following change of variables:

$$\xi = \lambda z, \quad \psi = \lambda\Psi, \quad \zeta = \omega/\lambda. \tag{30}$$

This transformation stretches the thin boundary layer and rescales the stream function and vorticity. The rescaling of the vorticity is also suggested from the similarity solution given by (28), while the corresponding rescaling of the stream function follows immediately from Eq. (21). It has also been used successfully in other studies such as Staniforth [17], Badr and Dennis [18], D'Alessio et al. [19] and D'Alessio and Kocabiyik [20], to list a few. It is worth pointing out that while ϕ could also be rescaled like ζ, the boundary conditions $\phi(\xi=0,\theta,t) = 1$ and $\phi\to 0$ as $\xi\to\infty$ suggest that ϕ is $O(1)$ and so rescaling ϕ is not necessary. In terms of these new variables, Eqs. (5)–(7) now become

$$\frac{\partial^2\Psi}{\partial z^2} + \lambda^2\frac{\partial^2\Psi}{\partial\theta^2} = M^2\omega, \tag{31}$$

$$\begin{aligned} & \frac{1}{M^2}\frac{\partial^2\omega}{\partial z^2} + 2z\frac{\partial\omega}{\partial z} + 2\omega \\ & \quad = 4t\frac{\partial\omega}{\partial t} - \frac{\lambda^2}{M^2}\frac{\partial^2\omega}{\partial\theta^2} - \frac{4t}{M^2}\left(\frac{\partial\Psi}{\partial\theta}\frac{\partial\omega}{\partial z} - \frac{\partial\Psi}{\partial z}\frac{\partial\omega}{\partial\theta}\right) \\ & \qquad - \frac{4t}{M^2}Ra\left(A\frac{\partial\phi}{\partial z} - B\lambda\frac{\partial\phi}{\partial\theta}\right), \end{aligned} \tag{32}$$

$$\frac{1}{PrM^2}\frac{\partial^2\phi}{\partial z^2}+2z\frac{\partial\phi}{\partial z}=4t\frac{\partial\phi}{\partial t}-\frac{\lambda^2}{PrM^2}\frac{\partial^2\phi}{\partial\theta^2}-\frac{4t}{M^2}\left(\frac{\partial\Psi}{\partial\theta}\frac{\partial\phi}{\partial z}-\frac{\partial\Psi}{\partial z}\frac{\partial\phi}{\partial\theta}\right) \tag{33}$$

and will be used to dictate the early stages of the flow and heat transfer process. We emphasize that although the boundary-layer coordinate, z, is utilized, the full Navier–Stokes and energy equations are to be solved and not the corresponding boundary-layer equations.

If R is large and t is small, then λ is also small, and it is possible to expand the flow variables in a double series in both λ and t as follows

$$\begin{aligned}\Psi&=(\Psi_{00}+t\Psi_{01}+\cdots)+\lambda(\Psi_{10}+t\Psi_{11}+\cdots)+O(\lambda^2),\\ \omega&=(\omega_{00}+t\omega_{01}+\cdots)+\lambda(\omega_{10}+t\omega_{11}+\cdots)+O(\lambda^2),\\ \phi&=(\phi_{00}+t\phi_{01}+t^2\phi_{02}+\cdots)+\lambda(\phi_{10}+t\phi_{11}+\cdots)\\ &\quad+O(\lambda^2).\end{aligned} \tag{34}$$

The need for the double series becomes apparent when the equations to $O(\lambda)$ are examined. These equations are still too complicated to solve analytically, and so an expansion in t is also necessary to make analytical progress. We point out, though, that the expansion in t is actually suggested by the solution given by (28). It would have been ideal if only a single series would suffice as this would relax the restriction for small t. A single expansion in the parameter λ would only require that λ be small which can be achieved for larger times provided that R is sufficiently large. We also note that the series given by (34) results in a regular perturbation problem as opposed to a singular perturbation problem. This is an added advantage of working in terms of the scaled flow variables and coordinates. The solutions given by (26) and (28) emerge naturally from this expansion procedure as we will point out. Also, as previously mentioned, complexity of the solution is greatly reduced when $Pr=1$. Therefore we will limit our analysis to this special case.

In order to proceed with this expansion procedure we will also need to expand the quantities $e^{-n\lambda z}$, A, B and M^2 in a similar series. This yields

$$\begin{aligned}e^{-n\lambda z}&=1-n\lambda z+\frac{n^2\lambda^2z^2}{2}-\cdots,\\ A(z,\theta)&=A_0(\theta)+\lambda zA_1(\theta)+\frac{\lambda^2z^2}{2}A_0(\theta)+\cdots,\\ B(z,\theta)&=B_0(\theta)+\lambda zB_1(\theta)+\frac{\lambda^2z^2}{2}B_0(\theta)+\cdots,\\ M^2(z,\theta)&=M_0^2(\theta)+\sinh(2\xi_0)\lambda z+\cosh(2\xi_0)\lambda^2z^2+\cdots,\end{aligned} \tag{35}$$

where $M_0^2(\theta)$ and $A_0(\theta)$ are defined according to (24) and (25) respectively while $A_1(\theta)$, $B_0(\theta)$ and $B_1(\theta)$ are given by

$$\begin{aligned}A_1(\theta)&=\cosh\xi_0\cos\eta\cos\theta-\sinh\xi_0\sin\eta\sin\theta,\\ B_0(\theta)&=\cosh\xi_0\cos\eta\sin\theta+\sinh\xi_0\sin\eta\cos\theta,\\ B_1(\theta)&=\sinh\xi_0\cos\eta\sin\theta+\cosh\xi_0\sin\eta\cos\theta.\end{aligned} \tag{36}$$

Substituting these expansions into Eqs. (31)–(33) and equating like powers of λ and t leads to a hierarchy of problems at various levels of approximation. We have explicitly determined the nonzero terms Ψ_{01}, ω_{01}, ϕ_{00}, ϕ_{02} and ϕ_{10} in the series (34) and have also deduced that $\Psi_{00}=\Psi_{10}=0$, $\omega_{00}=\omega_{10}=0$ and $\phi_{01}=0$. Rather than presenting all the tedious details, which can be found in [21], we will demonstrate the procedure for the $O(t)$ problem. Lastly, if $\Phi=\lambda\phi$ is used in place of ϕ then it has been proved that

$$\Phi_{00}=\Phi_{01}=\cdots=\Phi_{0n}=0\quad\text{for all } n, \tag{37}$$

which confirms that the rescaling of ϕ is unnecessary.

3.1. The O(t) problem

Collecting terms of order t in Eqs. (31) and (32) yields the system

$$\frac{1}{M_0^2}\frac{\partial^2\Psi_{01}}{\partial z^2}=\omega_{01}, \tag{38}$$

$$\frac{1}{M_0^2}\frac{\partial^2\omega_{01}}{\partial z^2}+2z\frac{\partial\omega_{01}}{\partial z}-2\omega_{01}=-\frac{4RaA_0}{M_0^2}\frac{\partial\phi_{00}}{\partial z}. \tag{39}$$

In order to solve this system an equation for ϕ_{00}, which comes from the $O(1)$ problem, is required; this equation, with $Pr=1$, reads

$$\frac{1}{M_0^2}\frac{\partial^2\phi_{00}}{\partial z^2}+2z\frac{\partial\phi_{00}}{\partial z}=0. \tag{40}$$

The solution satisfying $\phi_{00}=1$ on $z=0$ and $\phi_{00}\to0$ as $z\to\infty$ is

$$\phi_{00}(z,\theta)=\operatorname{erfc}(M_0z), \tag{41}$$

which is in full agreement with the previous solution given by (26). When this is substituted into Eq. (39) the following general solution for $\Omega_{01}=M_0\omega_{01}$ emerges:

$$\Omega_{01}(s,\theta)=C(\theta)s+D(\theta)(e^{-s^2}+\sqrt{\pi}s\operatorname{erf}(s))-\frac{2RaA_0}{\sqrt{\pi}}e^{-s^2}, \tag{42}$$

where $C(\theta)$, $D(\theta)$ are arbitrary functions of θ and $s=M_0z$. Imposing the far-field condition $\Omega_{01}\to0$ as $s\to\infty$ reveals that $C(\theta)=-\sqrt{\pi}D(\theta)$. The remaining unknown function $D(\theta)$ is to be determined by satisfying the integral conditions, which for Ω_{01} are as follows:

$$\int_0^\infty\int_0^{2\pi}\Omega_{01}\sin(n\theta)\,\mathrm{d}\theta\,\mathrm{d}s=\pi\mathrm{e}^{\xi_0}\cos\eta\delta_{1,n},\quad n=1,2,\ldots,$$
$$\int_0^\infty\int_0^{2\pi}\Omega_{01}\cos(n\theta)\,\mathrm{d}\theta\,\mathrm{d}s=\pi\mathrm{e}^{\xi_0}\sin\eta\delta_{1,n},\quad n=0,1,2,\ldots \tag{43}$$

The final solution becomes

$$\Omega_{01}(s,\theta)=\frac{1}{\sqrt{\pi}}[4\mathrm{e}^{\xi_0}\sin(\theta+\eta)+2RaA_0]\mathrm{e}^{-s^2}-4[\mathrm{e}^{\xi_0}\sin(\theta+\eta)+RaA_0]s\mathrm{erfc}(s). \tag{44}$$

This solution is equivalent in form to the solution given in (28). Lastly, the corresponding stream function, Ψ_{01}, is found by integrating

$$\frac{\partial^2\Psi_{01}}{\partial s^2}=\omega_{01}, \tag{45}$$

twice, subject to the boundary conditions $\Psi_{01}=0$ and $\partial\Psi_{01}/\partial s=0$ on $s=0$. The resulting solution is

$$\Psi_{01}(s,\theta)=\frac{\mathrm{e}^{\xi_0}}{M_0}\sin(\theta+\eta)s\mathrm{erf}(s)-\frac{2}{3M_0}[\mathrm{e}^{\xi_0}\sin(\theta+\eta)+RaA_0]s^3\mathrm{erfc}(s)+\frac{1}{3M_0}[2\mathrm{e}^{\xi_0}\sin(\theta+\eta)-RaA_0]\left[\frac{\mathrm{e}^{-s^2}-1}{\sqrt{\pi}}\right]+\frac{2}{3\sqrt{\pi}M_0}\left[\mathrm{e}^{\xi_0}\sin(\theta+\eta)+RaA_0\right]s^2\mathrm{e}^{-s^2}. \tag{46}$$

It is important to note that the above solution violates the far-field condition. This points to a weakness associated with this perturbation procedure; namely that one satisfies the no-slip and impermeability boundary conditions at the expense of the far-field condition. It must be remembered, though, that it is much more important to satisfy the surface conditions, since this leads to a more accurate solution near the cylinder surface where vorticity is generated. The consequence of not fully satisfying the far-field condition is judged to be negligible. The problem could be addressed by using a matched asymptotic solution, in which case the expression for Ψ_{01} (representing the inner solution) would have to be matched to a corresponding outer solution satisfying the far-field condition. As one can imagine, a matched asymptotic solution approach would require a lot more work with very little benefit since we are primarily interested in what is happening near the surface. Lastly, we emphasize that the vorticity is constructed in such a way that the far-field condition, $\omega\to 0$, is automatically obeyed. This is because the integral conditions make use of the far-field conditions for the stream function.

Repeating this procedure we have found that:

$$\phi_{10}(s,\theta)=-\frac{\sinh(2\xi_0)}{2M_0^3}\left[\frac{s}{2}\mathrm{erfc}(s)+\frac{s^2}{\sqrt{\pi}}\mathrm{e}^{-s^2}\right], \tag{47}$$

$$\phi_{02}(s,\theta)=\left(s^4+3s^2+\frac{3}{4}\right)\left[\int_0^s\frac{K(x,\theta)\mathrm{e}^{-x^2}}{(x^4+3x^2+3/4)^2}\mathrm{d}x-\frac{3}{\sqrt{\pi}}\int_0^\infty\frac{K(x,\theta)\mathrm{e}^{-x^2}}{(x^4+3x^2+3/4)^2}\mathrm{d}x\times\int_0^s\frac{\mathrm{e}^{-x^2}}{(x^4+3x^2+3/4)^2}\mathrm{d}x\right], \tag{48}$$

where $K(x,\theta)$ is a complicated function given by

$$\begin{aligned}K(x,\theta)&=\frac{8E_1(\theta)}{\sqrt{\pi}M_0^2}\left[\left(\frac{x^6}{6}+\frac{3x^4}{4}+\frac{3x^2}{8}+\frac{11}{64}\right)\mathrm{erf}(x)-\left(\frac{x^8}{12}+\frac{x^6}{3}+\frac{x^4}{8}\right)\mathrm{erfc}(x)-\frac{1}{\sqrt{\pi}}\left(\frac{2x^5}{15}+\frac{2x^3}{3}+\frac{x}{2}\right)+\frac{1}{\sqrt{\pi}}\left(\frac{x^7}{12}+\frac{11x^5}{24}+\frac{11x^3}{16}+\frac{5x}{32}\right)\mathrm{e}^{-x^2}\right]\\&+\frac{8E_2(\theta)}{3\sqrt{\pi}M_0^2}\left[\frac{1}{\sqrt{\pi}}\left(\frac{x^5}{5}+x^3+\frac{3x}{4}\right)-\frac{51}{64}\mathrm{erf}(x)-\left(\frac{x^8}{4}+x^6+\frac{3x^4}{8}\right)\mathrm{erfc}(x)+\frac{1}{\sqrt{\pi}}\left(\frac{x^7}{4}+\frac{7x^5}{8}+\frac{x^3}{16}+\frac{27x}{32}\right)\mathrm{e}^{-x^2}\right],\end{aligned} \tag{49}$$

where

$$E_1(\theta)=\mathrm{e}^{\xi_0}\left(\cos(\theta+\eta)-\frac{\sin(\theta+\eta)\sin(2\theta)}{2M_0^2}\right)$$

and

$$E_2(\theta)=Ra\left(\frac{\mathrm{d}A_0}{\mathrm{d}\theta}-\frac{A_0\sin(2\theta)}{2M_0^2}\right).$$

The solution for ω_{11} with $Ra=0$ has been found in [3]; however, for $Ra\neq 0$ the solution is quite complicated. Thus, the series solution becomes

$$\begin{aligned}\Psi&\sim t\Psi_{01},\\ \omega&\sim t\omega_{01},\\ \phi&\sim\phi_{00}+t^2\phi_{02}+\lambda\phi_{10}.\end{aligned} \tag{50}$$

This approximate solution should provide information sufficient to validate the numerical solution obtained by numerically integrating Eqs. (31)–(33), which is discussed in the following section.

4. Numerical solution procedure

From a numerical point of view, it is essential to introduce the scaling $\Phi=\lambda\phi$ since the initial temperature

distribution given by (20) is singular, and may therefore lead to numerical difficulties. In terms of the variable Φ the surface boundary condition becomes $\Phi = \lambda$ on $z = 0$ and the initial temperature distribution is simply $\Phi(z, \theta, t = 0) = 0$. The corresponding equation for Φ is given by

$$\frac{1}{PrM^2}\frac{\partial^2\Phi}{\partial z^2} + 2z\frac{\partial\Phi}{\partial z} + 2\Phi = 4t\frac{\partial\Phi}{\partial t} - \frac{\lambda^2}{PrM^2}\frac{\partial^2\Phi}{\partial\theta^2} - \frac{4t}{M^2}\left(\frac{\partial\Psi}{\partial\theta}\frac{\partial\Phi}{\partial z} - \frac{\partial\Psi}{\partial z}\frac{\partial\Phi}{\partial\theta}\right). \tag{51}$$

The numerical method implemented to solve Eqs. (31), (32) and (51) is a spectral-finite difference scheme and is an extension of that outlined in [3] to include the heat transfer equation. We begin by discretizing the computational domain bounded by $0 \leqslant z \leqslant z_\infty$ and $0 \leqslant \theta \leqslant 2\pi$ into a network of $N \times L$ grid points located at

$$z_i = ih, \quad i = 0, 1, \ldots, N, \tag{52}$$

$$\theta_j = jk, \quad j = 0, 1, \ldots, L, \tag{53}$$

with

$$h = \frac{z_\infty}{N}, \tag{54}$$

$$k = \frac{2\pi}{L}. \tag{55}$$

Here, z_∞ refers to the outer boundary approximating infinity. By placing z_∞ well outside the growing boundary layer, this enables us to enforce the far-field condition along the line $z = z_\infty$. Since the physical coordinate $\xi = \lambda z$ is a moving coordinate, the outer boundary $\xi_\infty = \lambda z_\infty$ is constantly being pushed further away from the cylinder surface. This justifies using the far-field condition along the outer boundary ξ_∞ for all times considered in this study.

The stream function is expanded in a truncated Fourier series given by

$$\Psi(z, \theta, t) = \frac{1}{2}F_0(z, t) + \sum_{n=1}^{N_f}[F_n(z, t)\cos n\theta + f_n(z, t)\sin n\theta]. \tag{56}$$

This transforms Eq. (31) into the following sets of equations for F_n and f_n:

$$\frac{\partial^2 f_n}{\partial z^2} - n^2\lambda^2 f_n = r_n(z, t); \quad n = 1, 2, \ldots, M, \tag{57}$$

$$\frac{\partial^2 F_n}{\partial z^2} - n^2\lambda^2 F_n = s_n(z, t); \quad n = 0, 1, \ldots, M. \tag{58}$$

The functions $r_n(z, t)$ and $s_n(z, t)$ are defined as

$$r_n(z, t) = \frac{1}{\pi}\int_0^{2\pi} M^2\omega\sin n\theta\,\mathrm{d}\theta; \quad n = 1, 2, \ldots, M, \tag{59}$$

$$s_n(z, t) = \frac{1}{\pi}\int_0^{2\pi} M^2\omega\cos n\theta\,\mathrm{d}\theta; \quad n = 0, 1, \ldots, M. \tag{60}$$

Boundary conditions for F_n and f_n follow from the no-slip, impermeability and the far-field conditions which become

$$F_0(0, t) = 0, \quad F_n(0, t) = 0, \quad f_n(0, t) = 0, \tag{61}$$

$$\frac{\partial F_0}{\partial z} = 0, \quad \frac{\partial F_n}{\partial z} = 0, \quad \frac{\partial f_n}{\partial z} = 0 \text{ on } z = 0 \text{ for all } t, \tag{62}$$

$$\mathrm{e}^{-\lambda z}F_0 \to 0, \quad \mathrm{e}^{-\lambda z}F_n \to \frac{1}{2\lambda}t\mathrm{e}^{\xi_0}\sin\eta\delta_{1,n},$$

$$\mathrm{e}^{-\lambda z}f_n \to \frac{1}{2\lambda}t\mathrm{e}^{\xi_0}\cos\eta\delta_{1,n} \text{ as } z \to \infty \tag{63}$$

and

$$\mathrm{e}^{-\lambda z}\frac{\partial F_0}{\partial z} \to 0, \quad \mathrm{e}^{-\lambda z}\frac{\partial F_n}{\partial z} \to \frac{1}{2}t\mathrm{e}^{\xi_0}\sin\eta\delta_{1,n},$$

$$\mathrm{e}^{-\lambda z}\frac{\partial f_n}{\partial z} \to \frac{1}{2}t\mathrm{e}^{\xi_0}\cos\eta\delta_{1,n} \text{ as } z \to \infty, \tag{64}$$

for $n = 1, 2, \ldots, N_f$. Lastly, the integral conditions can be formulated in terms of $r_n(z, t)$ and $s_n(z, t)$ as follows:

$$\int_0^\infty \mathrm{e}^{-n\lambda z}r_n(z, t)\,\mathrm{d}z = t\mathrm{e}^{\xi_0}\cos\eta\delta_{1,n}, \tag{65}$$

$$\int_0^\infty \mathrm{e}^{-n\lambda z}s_n(z, t)\,\mathrm{d}z = t\mathrm{e}^{\xi_0}\sin\eta\delta_{1,n}, \tag{66}$$

$$\int_0^{z_\infty} s_0(z, t)\,\mathrm{d}z = 0. \tag{67}$$

Eqs. (57) and (58) at a fixed value of t are of the form

$$h''(z) - \beta^2 h(z) = p(z), \tag{68}$$

where $\beta = n\lambda$ and the prime refers to differentiation with respect to z. These ordinary differential equations can be integrated using step-by-step formulae. The important point to note here is that the particular marching algorithm to be used is dependent on the parameter β. Dennis and Chang [22] have found that most step-by-step procedures become increasingly unstable as β becomes large. Hence, two sets of step-by-step methods were utilized: one for $\beta < 0.5$ while another one for $\beta \geqslant 0.5$. The specific schemes used will not be presented; however, these details can be found in Staniforth [17].

The vorticity and heat transport equations (32) and (51) are solved by finite differences. The scheme used to approximate these equations is very similar to the Crank–Nicolson implicit procedure. These equations may be cast in the generic form given by

$$t\frac{\partial\chi}{\partial t} = q(z, \theta, t), \tag{69}$$

where χ represents either ω or Φ and q the corresponding right-hand side. Assuming the solution at time t is

known, let us advance the solution to time $t+\Delta t$ by integrating Eq. (69). Integration by parts yields

$$\chi\tau|_t^{t+\Delta t} - \int_t^{t+\Delta t} \chi \,\mathrm{d}\tau = \int_t^{t+\Delta t} q \,\mathrm{d}\tau, \tag{70}$$

where Δt is the time increment. Approximation of the integrals using the trapezoidal rule yields the expression

$$\chi(z,\theta,t+\Delta t) = \chi(z,\theta,t) + \left(\frac{\Delta t}{2t+\Delta t}\right) \times [q(z,\theta,t+\Delta t) + q(z,\theta,t)]. \tag{71}$$

Since $q(z,\theta,t+\Delta t)$ depends on $\omega(z,\theta,t+\Delta t)$ or $\Phi(z,\theta,t+\Delta t)$ and their spatial derivatives, the scheme is implicit. Eq. (71) is solved iteratively using the Gauss–Seidel procedure where all spatial derivatives appearing in q are approximated using central differences.

The boundary conditions used in solving the vorticity transport equation include

$$\omega(z,\theta,t) = \omega(z,\theta+2\pi,t) \quad \text{and} \quad \omega(z_\infty,\theta,t) = 0, \tag{72}$$

while for the heat transport equation we impose

$$\Phi(z=0,\theta,t) = \lambda, \Phi(z,\theta,t) = \Phi(z,\theta+2\pi,t) \quad \text{and} \quad \Phi(z_\infty,\theta,t) = 0. \tag{73}$$

The surface vorticity can be determined by inverting (59) and (60); this leads to

$$\omega(0,\theta,t) = \frac{1}{M_0^2}\left\{\frac{1}{2}s_0(0,t) + \sum_{n=1}^{N_f}[r_n(0,t)\sin n\theta + s_n(0,t)\cos n\theta]\right\}. \tag{74}$$

To initiate the integration procedure we use the initial conditions for Ψ, ω and Φ which are provided by the analytical solution. These are the trivial solutions

$$\Psi(z,\theta,t=0) = \omega(z,\theta,t=0) = \Phi(z,\theta,t=0) = 0. \tag{75}$$

It may also be necessary to subject the surface vorticity to under-relaxation in order to obtain convergence. Convergence is reached when the difference between two successive iterates of the surface vorticity, $|\omega^{(k+1)}(0,\theta,t) - \omega^{(k)}(0,\theta,t)|$, falls below some specified tolerance ε. Also, the integrals appearing in (59) and (60) were evaluated by Filon integration [23] in order to guarantee consistent accuracy for all n. This technique bears a close resemblance to Simpson's rule with the exception that only the unknown numerically determined part of the integrand is approximated by a parabola over three successive grid points rather than the entire integrand. Lastly, we point out that the scheme described here is tailored to capture the essential physics of the early stages of the flow and heat transfer process.

5. Results and comparisons

The flow is characterized by the following dimensionless parameters: R, Ra, Pr, r and η. The numerical simulations carried out in this work focussed on the Reynolds number range 50–1000 with emphasis on $R = 500$. We have fixed the parameters Pr, r and η to assume the values $Pr = 1$, $\eta = 45°$ and $r = 0.5$ and have allowed the Rayleigh number to vary from 0 to 10. By restricting Ra to this range, the Boussinesq approximation should remain valid.

To confirm numerical convergence, computations were carried out using two different grids: a fine grid having $N \times L = 161 \times 121$, and a coarse grid having $N \times L = 101 \times 81$. In Fig. 2 the time variation of the drag coefficient, C_D, is shown using these different grids for the case $R = 500$ and $Ra = 1$. The diagram shows some dependence on the grid for $t > 2.5$; however, finer grids produced negligible additional change. Similar agreement was observed with the lift coefficient, C_L. Another important computational parameter is the outer boundary location z_∞. We have experimented with two different values of z_∞: $z_\infty = 6$ and $z_\infty = 10$. Displayed in Fig. 3 is a comparison in the time variation of the lift coefficient using these values of z_∞ again for the case $R = 500$ and $Ra = 1$. It is clear from Fig. 3 that the results are weakly dependent on z_∞. From these experiments and others we have decided to use the fine grid and $z_\infty = 10$ in our computations. Other computational parameters used include a relaxation parameter in the range 0.5–0.75, $N_f = 25$ terms of the Fourier series, and a typical tolerance value of $\varepsilon = 10^{-6}$. The number of terms retained in the series was suggested by examining the analytical solution. The analytical solution was also used to verify that the value of $z_\infty = 10$ was appropriate. Initial time steps of 10^{-4} were used for the first 10 advances. Then, the next 10 time steps were proceeded with $\Delta t = 10^{-3}$ and continued after with $\Delta t = 10^{-2}$. Further accuracy checks were conducted by comparing the numerical results with the analytical solution previously derived, and forms the main contribution of this study.

The dimensionless drag and lift coefficients were computed using the formulae

$$X = \frac{2\sinh\xi_0}{R}\int_0^{2\pi}\left(\frac{\partial\zeta}{\partial\xi}\right)_0 \sin(\theta)\,\mathrm{d}\theta - \frac{2\cosh\xi_0}{R} \times \int_0^{2\pi}\zeta_0\sin(\theta)\,\mathrm{d}\theta - \pi Ra\sinh\xi_0\cosh\xi_0\sin\eta, \tag{76}$$

$$Y = -\frac{2\cosh\xi_0}{R}\int_0^{2\pi}\left(\frac{\partial\zeta}{\partial\xi}\right)_0 \cos(\theta)\,\mathrm{d}\theta + \frac{2\sinh\xi_0}{R} \times \int_0^{2\pi}\zeta_0\cos(\theta)\,\mathrm{d}\theta - \pi Ra\sinh\xi_0\cosh\xi_0\cos\eta. \tag{77}$$

Since the above forces are directed along the x–y axis shown in Fig. 1, the dimensionless drag and lift

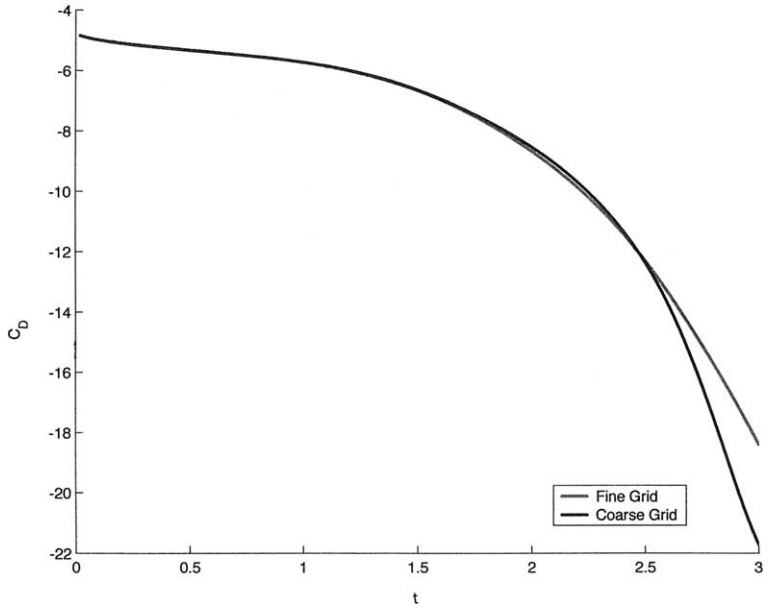

Fig. 2. Time variation of the drag coefficient using different grids for the case $R = 500$, $Ra = 1$.

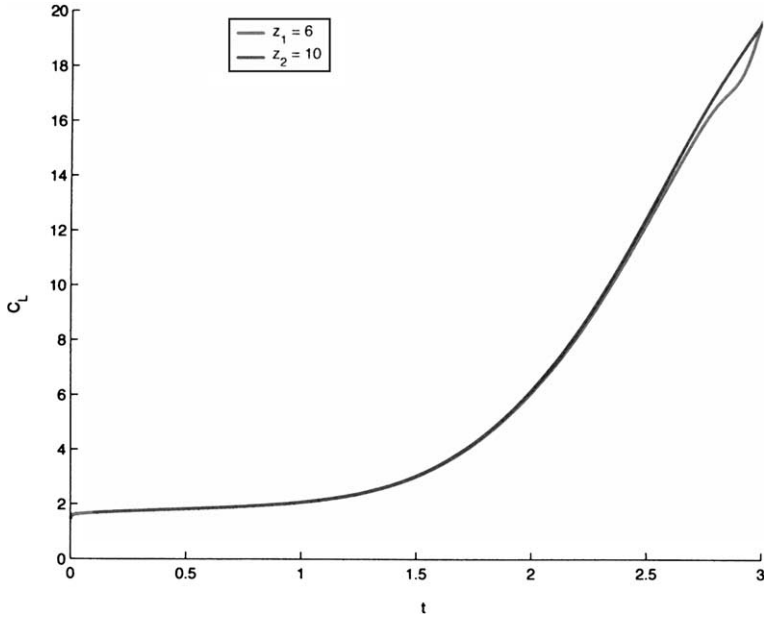

Fig. 3. Time variation of the lift coefficient using different outer boundary locations for the case $R = 500$, $Ra = 1$.

coefficients in the horizontal and vertical directions then become

$$C_{\mathrm{D}} = X\cos(\eta) - Y\sin(\eta), \tag{78}$$

$$C_{\mathrm{L}} = Y\cos(\eta) + X\sin(\eta). \tag{79}$$

A derivation of these formulae is included in the Appendix A. The heat transfer coefficients, Nu and $\overline{Nu}$, were determined using the formulae

$$Nu = -\frac{2}{M_0}\left(\frac{\partial\phi}{\partial\xi}\right)_{\xi=0},$$

$$\overline{Nu} = \frac{1}{2\pi}\int_0^{2\pi} Nu\,\mathrm{d}\theta. \tag{80}$$

5.1. Comparison of numerical results with analytical solution

While convergence of the numerical scheme has been demonstrated by comparing results using different grid sizes and outer boundary locations, we can further justify the numerics against the analytical solution found in Section 3. Additional checks were made by carrying out simulations with $Ra = 0$ and comparing the flow properties with those reported in [3]. Excellent agreement was obtained.

Using the approximation given by (50) for the vorticity, we are able to predict time variations for the drag and lift coefficients which will be valid for small times. These expressions become

$$\begin{aligned} C_{\mathrm{D}} \sim {} & -\pi(\sin^2\eta + \mathrm{e}^{\xi_0}\sinh\xi_0) - 2\mathrm{e}^{\xi_0}\sqrt{\frac{2t}{\pi R}} \\ & \times (a_1\cosh\xi_0\cos^2\eta + a_2\sinh\xi_0\sin^2\eta) \\ & + Ra\sin\eta\cos\eta\sqrt{\frac{2t}{\pi R}}(a_1\cosh^2\xi_0 - a_2\sinh^2\xi_0), \end{aligned} \tag{81}$$

$$\begin{aligned} C_{\mathrm{L}} \sim {} & \pi\sin\eta\cos\eta + 2\mathrm{e}^{\xi_0}\sin\eta\cos\eta\sqrt{\frac{2t}{\pi R}}(a_2\sinh\xi_0 \\ & - a_1\cosh\xi_0) + Ra\sqrt{\frac{2t}{\pi R}}(a_2\sinh^2\xi_0\cos^2\eta \\ & + a_1\cosh^2\xi_0\sin^2\eta), \end{aligned} \tag{82}$$

where

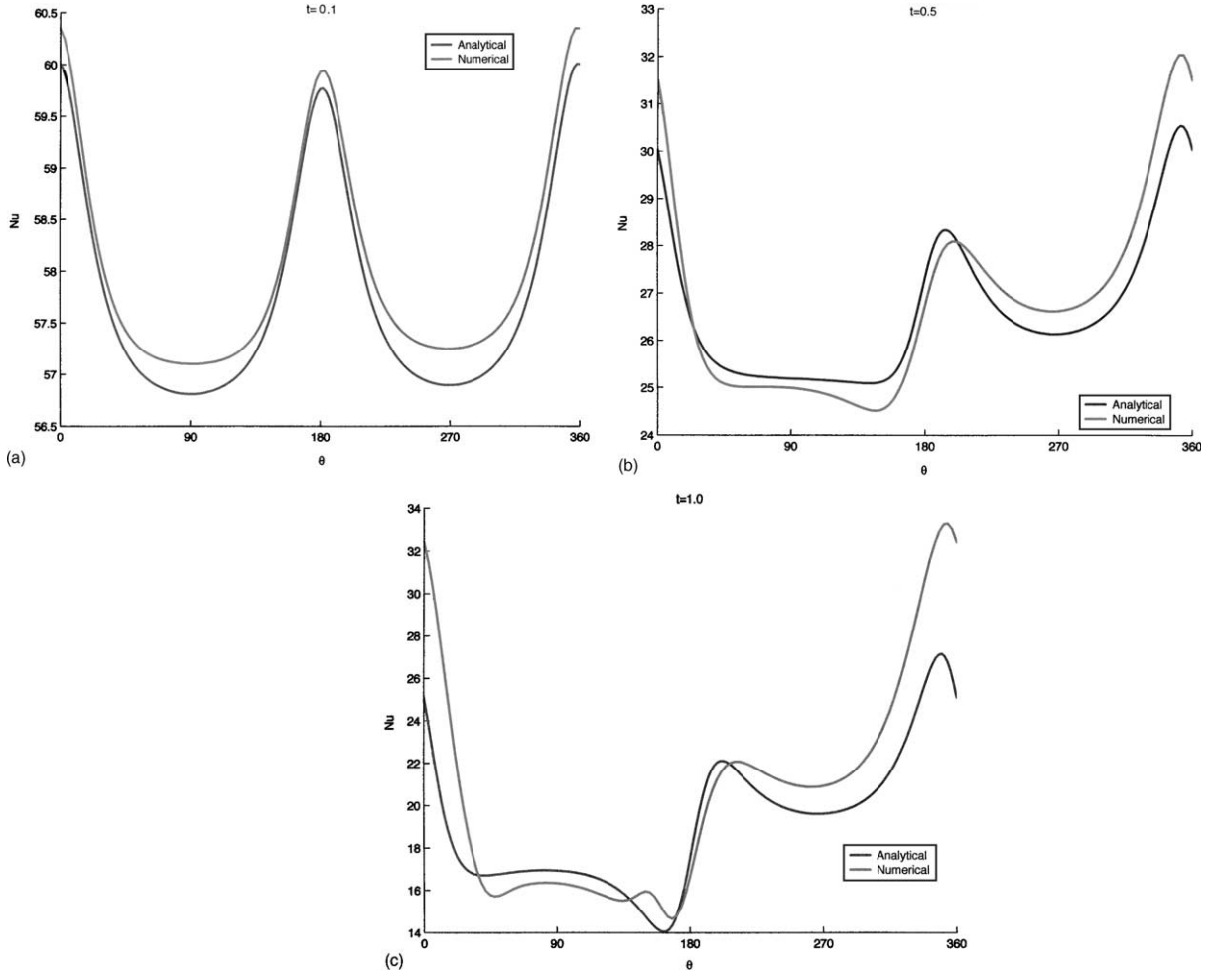

Fig. 4. Distributions of the Nusslet number for $R = 500$, $Ra = 1$ at times: (a) $t = 0.1$, (b) $t = 0.5$, and (c) $t = 1$.

$$a_1 = \int_0^{2\pi} \frac{\sin^2\theta}{M_0}\,\mathrm{d}\theta \simeq 3.1035$$

and

$$a_2 = \int_0^{2\pi} \frac{\cos^2\theta}{M_0}\,\mathrm{d}\theta \simeq 4.3668 \text{ for } r = \frac{1}{2}.$$

We can similarly derive formulae for Nu and $\overline{Nu}$ valid for small times. The following expressions emerge:

$$Nu(\theta,t) \sim \sqrt{\frac{2R}{\pi t}} + \frac{\sinh(2\xi_0)}{2M_0^3} + \sqrt{\frac{8Rt^3}{\pi}} \int_0^{\infty} \frac{K(s,\theta)\mathrm{e}^{-s^2}}{\left(s^4+3s^2+3/4\right)^2}\,\mathrm{d}s, \tag{83}$$

$$\overline{Nu}(t) \sim \frac{a_3 \sinh(2\xi_0)}{2} + \sqrt{\frac{2R}{\pi t}}, \tag{84}$$

where

$$a_3 = \frac{1}{2\pi}\int_0^{2\pi} \frac{\mathrm{d}\theta}{M_0^3} \simeq 2.0031 \text{ for } r = \frac{1}{2}.$$

It has been proved that

$$\int_0^{2\pi}\int_0^{\infty} \frac{K(s,\theta)\mathrm{e}^{-s^2}}{\left(s^4+3s^2+3/4\right)^2}\,\mathrm{d}s\,\mathrm{d}\theta = 0 \quad \text{for all } 0 < r < 1.$$

Note that at $t = 0$ both Nu and $\overline{Nu}$ are singular; this is due to the initial configuration. At $t = 0$ the surface is held at T_0 while the surrounding fluid is fixed at T_∞. This means that the temperature gradient on the surface will initially be infinite. With the passage of time this gradient rapidly decays due to molecular diffusion. Also, at this level of approximation $\overline{Nu}(t)$ does not depend explicitly on Ra while $Nu(\theta,t)$ does, by virtue of the function $K(s,\theta)$ (see Eq. (49)). This finding is supported by our numerical simulations.

We next present comparisons between the analytical predictions and the numerical results for the case $Ra = 1$ and $R = 500$ (as previously stated $Pr = 1$, $r = 0.5$ and $\eta = 45^\circ$ for all simulations). Contrasted in Fig. 4a–c are distributions of $Nu(\theta,t)$ at times $t = 0.1$, 0.5, 1 respectively. Initially, the rate of heat transfer is the same on the top and bottom halves of the cylinder, but the plots at later times reveal that this symmetry is short lived. The agreement between the analytical and numerical solutions is quite reasonable even at $t = 1$. The time variation of the average Nusselt number, portrayed in Fig. 5, exhibits a rapid algebraic decrease in $\overline{Nu}(t)$ with excellent agreement between the two solutions. Illustrated in Fig. 6a–c are scaled surface vorticity plots at times $t = 0.1$, 0.5, 1 respectively. These distributions clearly reveal how the agreement between the analytical and numerical solutions worsens as time marches on. This type of agreement is to be expected and the reason it is more evident in the surface vorticity plots than it is in the Nu plots is likely the fact that only one term in the vorticity series was found compared to the three terms found in the temperature series. Lastly, displayed in Fig. 7a and b are time variations of the drag and lift coefficients respectively. Included in Fig. 7a is a semi-analytical $O(\sqrt{t})$ correction to improve the agreement with the fully numerical result.

We next present more numerical results beginning with the case of forced convection.

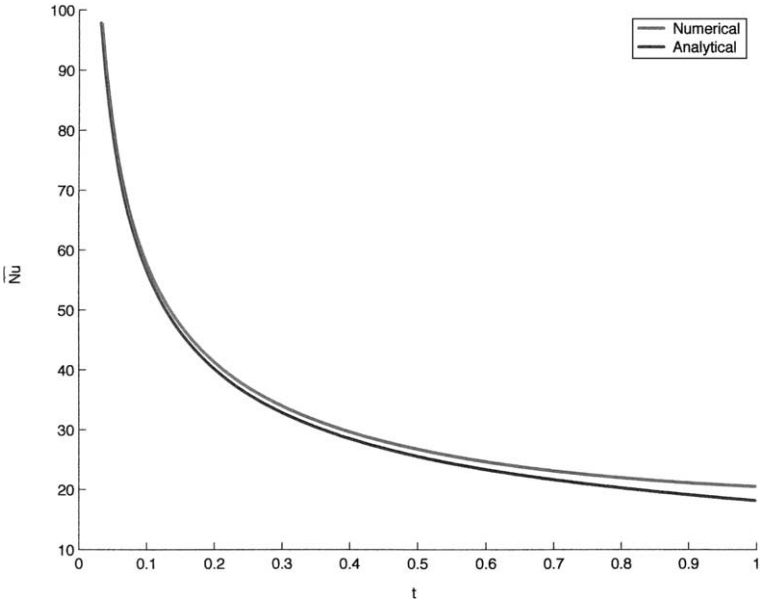

Fig. 5. Time variation of the average Nusslet number for $R = 500$, $Ra = 1$.

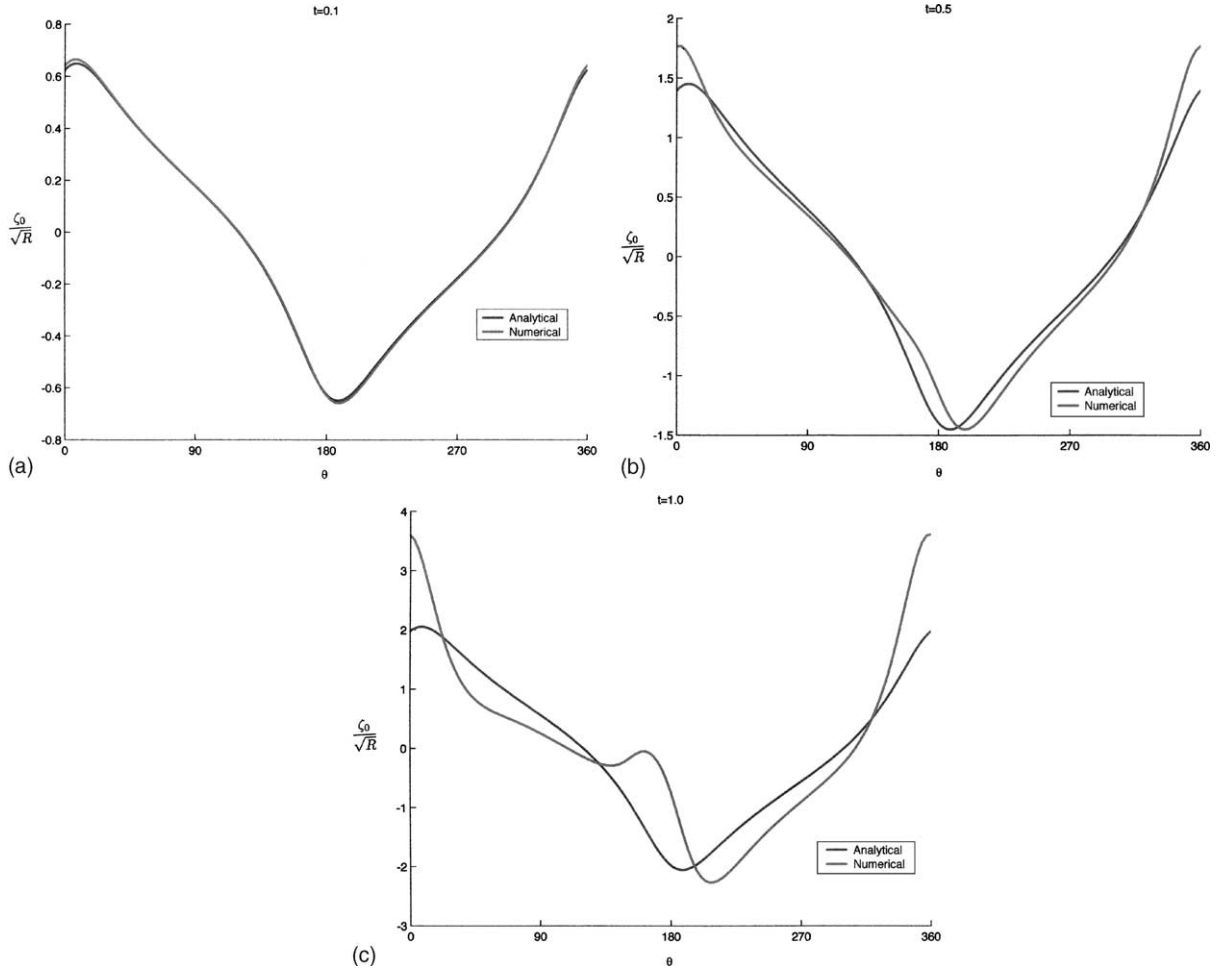

Fig. 6. Distributions of the surface vorticity for $R = 500$, $Ra = 1$ at times: (a) $t = 0.1$, (b) $t = 0.5$ and (c) $t = 1$.

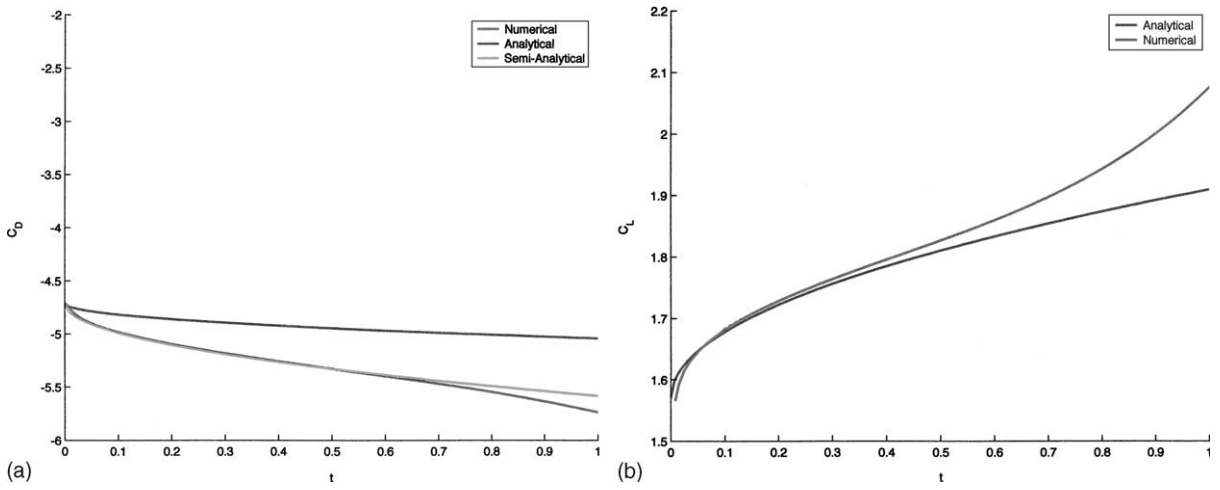

Fig. 7. Time variation of the (a) drag and (b) lift coefficients for $R = 500$, $Ra = 1$.

5.2. Forced convection case

Forced convection is a limiting case having $Ra = 0$. In forced convection the temperature equation becomes decoupled from the Navier–Stokes equations; consequently, the heat transfer process has no influence on the flow, and the temperature can be computed after the flow field has been determined.

We have carried out simulations for $R = 100$, 500, 1000 and have observed a weak dependence on R for this Reynolds number range. Streamline plots for the case $R = 500$ are shown in Fig. 8a–e (while the cases $R = 100$ and $R = 1000$ are included in [3]). In all streamline plots to be presented the values of the streamlines plotted from top to bottom in each diagram correspond to:

$$\psi = 0.9, 0.8, 0.7, 0.6, 0.5, 0.4, 0.3, 0.2, 0.1, 0.05, 0, -0.05, -0.1, -0.2, -0.3, -0.4, -0.5, -0.6, -0.7, -0.8, -0.9.$$

The plots reveal that vortex shedding from the trailing tip takes place between $t = 1$ and $t = 1.5$ and that a vortex forms and grows on the top half of the cylinder during the interval $2 < t < 3$. Also apparent is that the spacing between consecutive streamlines decreases with time due to the continually increasing far-field velocity.

The isotherm plots shown in Fig. 9a–e further support the flow features. In all isotherm plots to be pre-

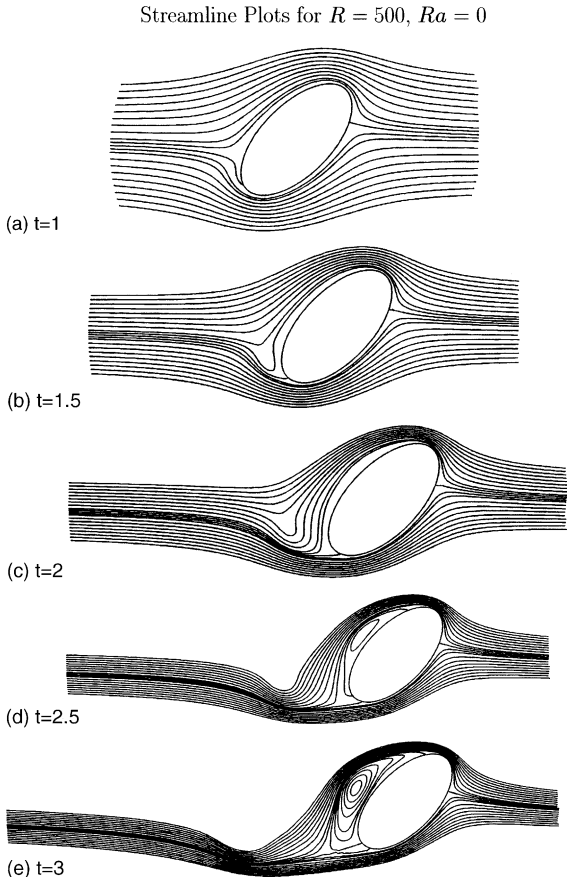

Fig. 8. Streamline plots for $R = 500$, $Ra = 0$ at times: (a) $t = 1$, (b) $t = 1.5$, (c) $t = 2$, (d) $t = 2.5$ and (e) $t = 3$.

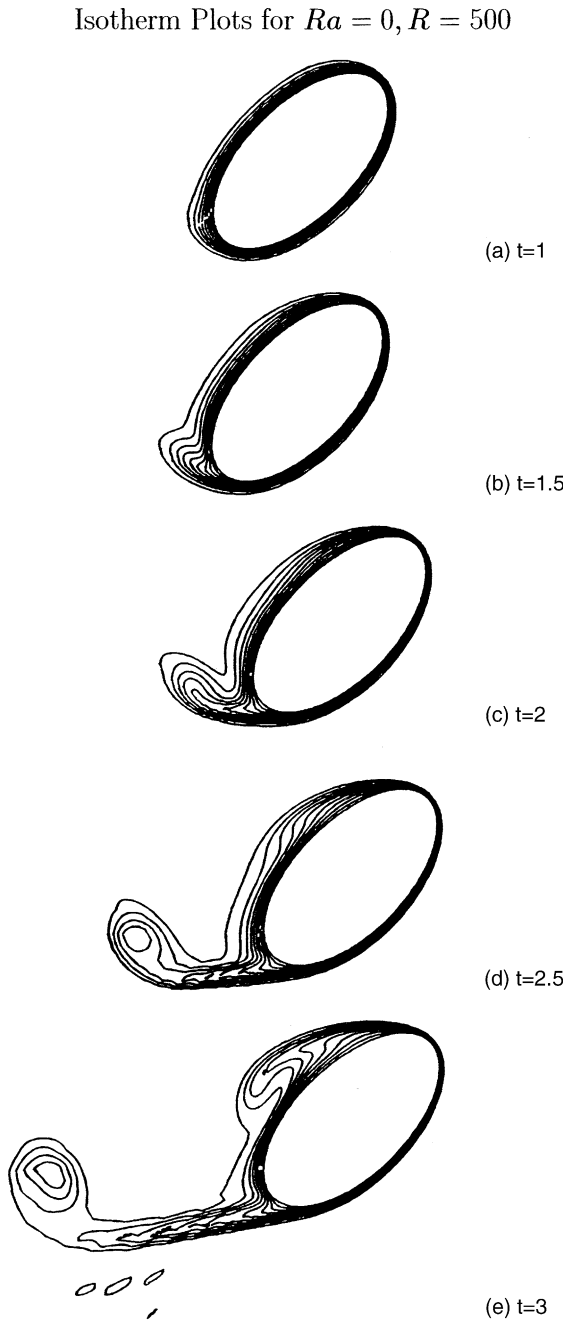

Fig. 9. Isotherm plots for $R = 500$, $Ra = 0$ at times: (a) $t = 1$, (b) $t = 1.5$, (c) $t = 2$, (d) $t = 2.5$ and (e) $t = 3$.

sented, the difference in temperature between consecutive contours is 0.1; the outermost contour corresponds to $\phi = 0.2$, and the innermost contour denotes the cylinder surface maintained at $\phi = 1$. The plots illustrate the formation of a thermal wake and the vortex shedding process, and that the rate of heat transfer is greatest at the leading tip and bottom half of the ellipse.

Displayed in Figs. 10 and 11 are distributions of Nusselt number and surface vorticity respectively for $R = 500$ at various times. These plots illustrate how

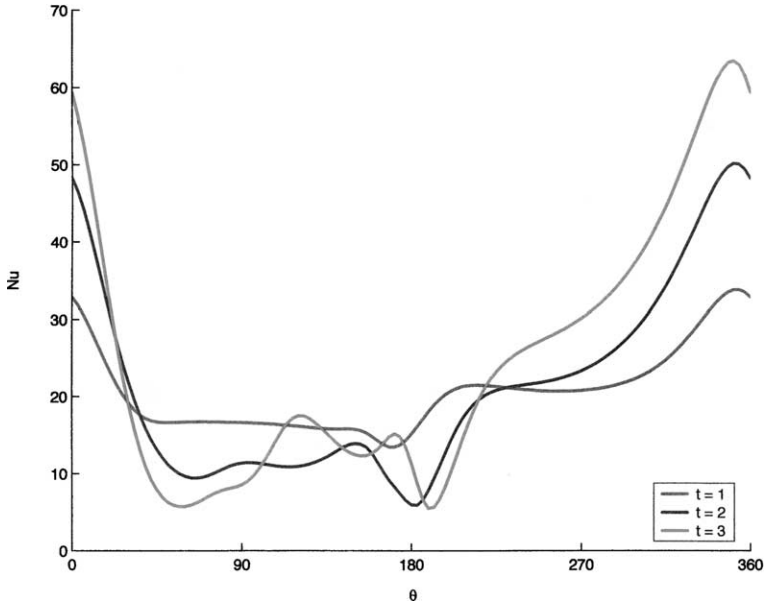

Fig. 10. Distributions of the Nusselt number for $R = 500$, $Ra = 0$ at times $t = 1, 2, 3$.

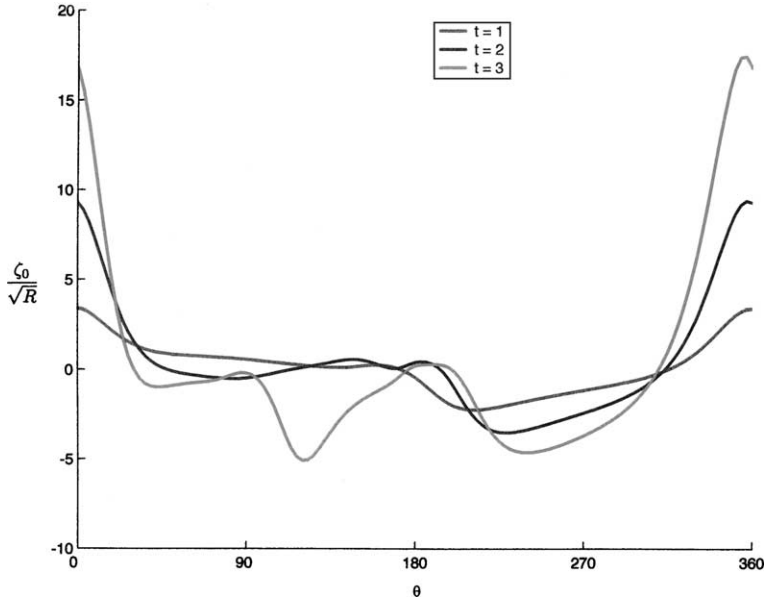

Fig. 11. Distributions of the surface vorticity for $R = 500$, $Ra = 0$ at times $t = 1, 2, 3$.

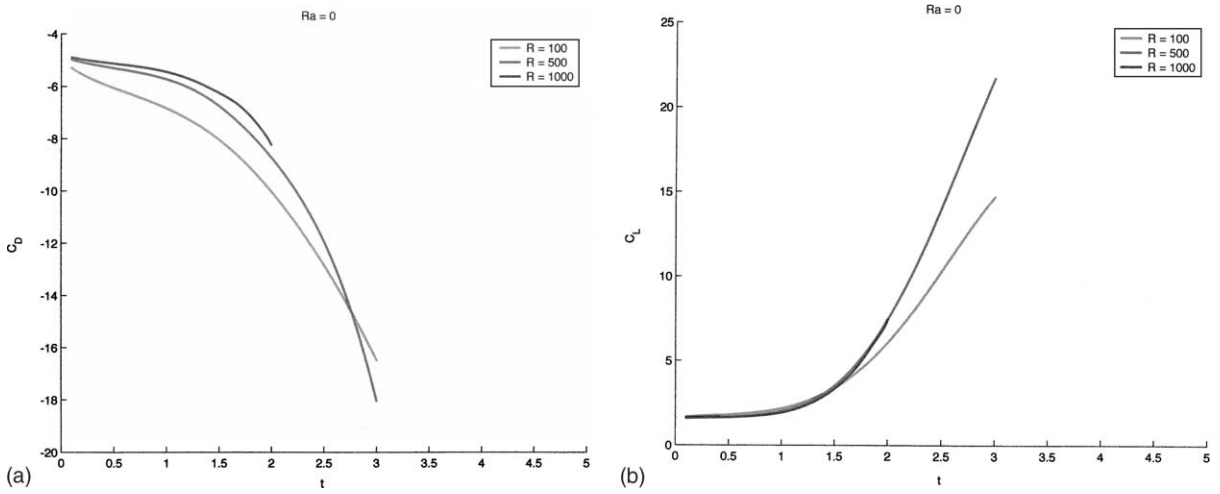

Fig. 12. Time variation of the (a) drag and (b) lift coefficients for $R = 100$, 500, 1000 with $Ra = 0$.

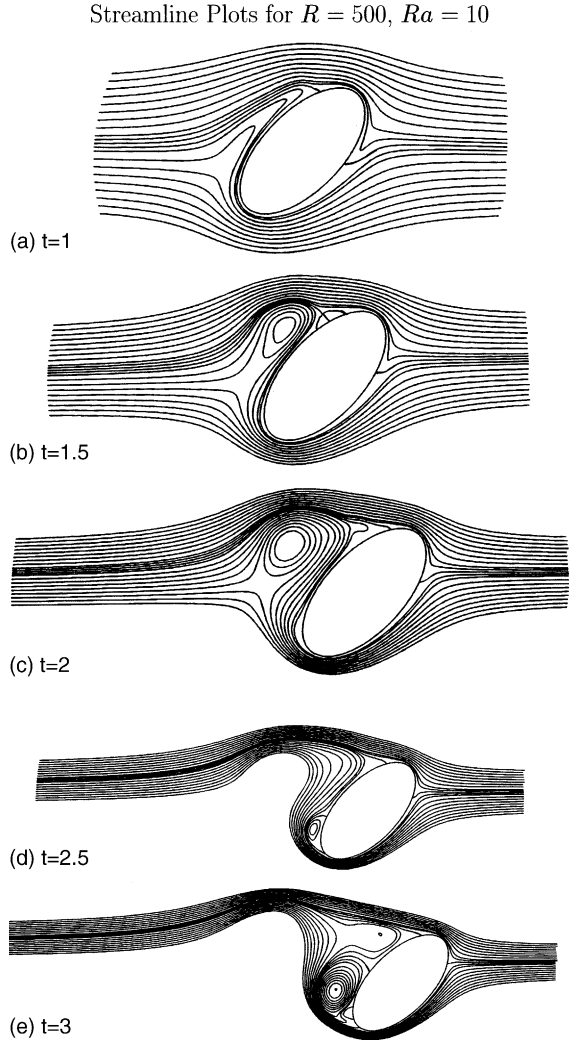

Fig. 13. Streamline plots for $R = 500$, $Ra = 10$ at times: (a) $t = 1$, (b) $t = 1.5$, (c) $t = 2$, (d) $t = 2.5$ and (e) $t = 3$.

surface variations become more pronounced in the vicinity of the tips as time elapses. Shown in Fig. 12a and b are time variations of the drag and lift coefficients respectively for $R = 100$, 500, 1000. These plots reveal an initially slow decrease (increase) followed by a much more rapid decrease (increase) after $t = 1$ in C_D (C_L). They also show little dependence on R, especially between $R = 500$ and $R = 1000$.

5.3. Mixed convection case

To study the case of mixed convection we first fixed the Reynolds number to $R = 500$ and varied the Rayleigh number. To understand the influence on the rate of heat transfer, simulations were carried out for the values $Ra = 1$, 5, 10. Little change between the forced convection case and that having $Ra = 1$ was found. The only difference worth mentioning is that vortex shedding from the trailing tip was delayed.

Significant changes during the initial stages of the flow were apparent when Ra was increased further to 5 and 10. Some common features noticed for $Ra = 5$, 10 are as follows. Buoyancy forced the fluid to flow around the trailing tip rather than getting advected downstream. Also, shed vortices tended initially to rise with negligible advection due to the blockage provided by the cylinder. Further, shed vortices began to interact with each other forming counter-rotating vortex pairs. Merging of vortices did not take place; instead, the vortex pair grew to the stage where the cylinder could no longer shield them from the oncoming flow. Consequently, they slowly made their way downstream. Increasing Ra enhanced the buoyancy force which reduced the rising time of the shed vortices and delayed vortex shedding. The outcome of this is that less interaction between the shed vortices was noticed for $Ra = 10$ compared to $Ra = 5$. Fig. 13a–e illustrate the above features for the case $Ra = 10$. The

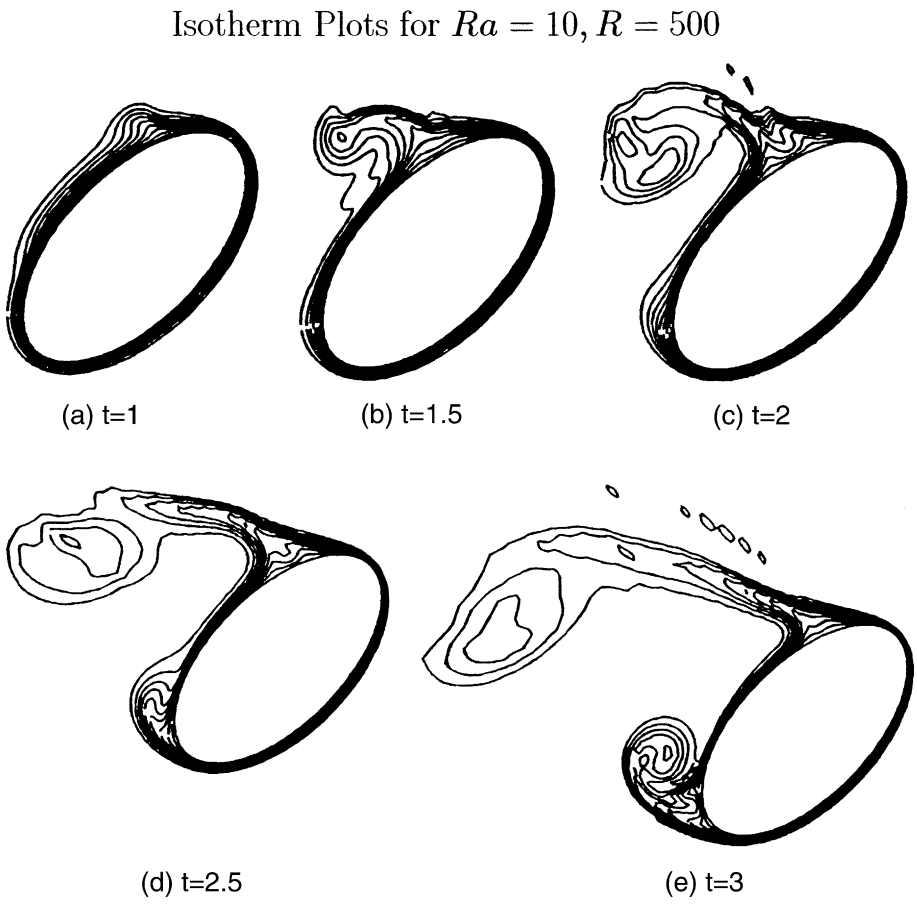

Fig. 14. Isotherm plots for $R = 500$, $Ra = 10$ at times: (a) $t = 1$, (b) $t = 1.5$, (c) $t = 2$, (d) $t = 2.5$ and (e) $t = 3$.

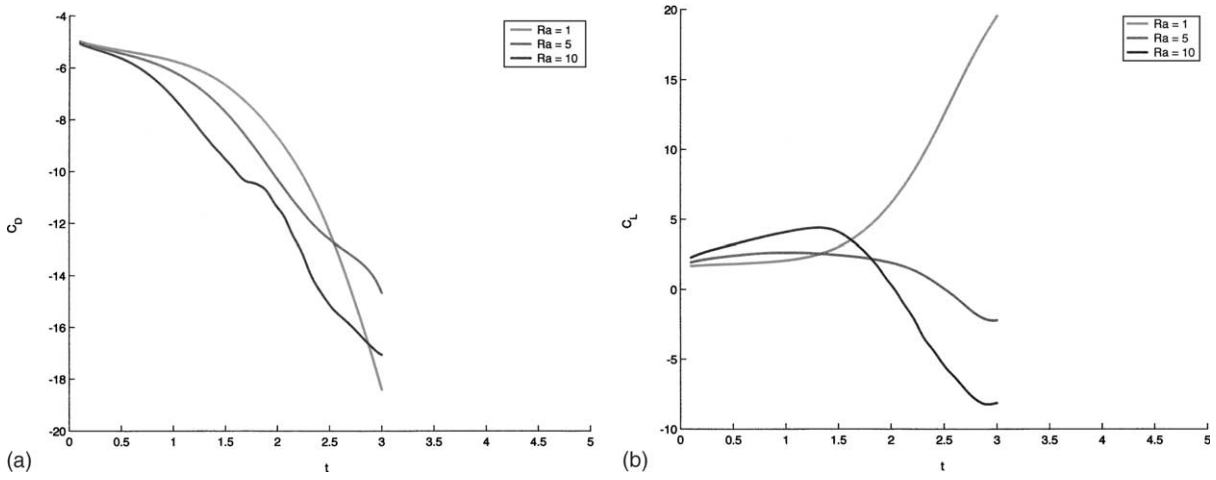

Fig. 15. Time variation of the (a) drag and (b) lift coefficients for $Ra = 1$, 5, 10 with $R = 500$.

corresponding isotherm plots, displayed in Fig. 14a–e, clearly portray the formation and eruption of a thermal plume from the surface near the leading tip. The thermal plume is seen to extend downstream beyond the thermal wake. The thermal plume also had obvious impacts on the Nusselt number and surface vorticity distributions.

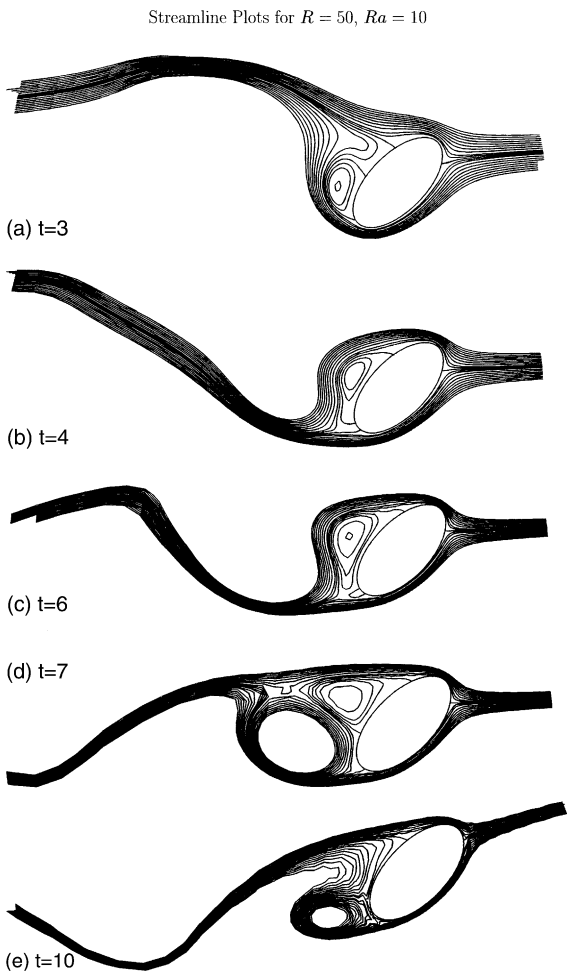

Fig. 16. Streamline plots for $R = 50$, $Ra = 10$ at times: (a) $t = 3$, (b) $t = 4$, (c) $t = 6$, (d) $t = 7$ and (e) $t = 10$.

Shown in Fig. 15a–b are time variations of the drag and lift coefficients respectively, for $Ra = 1$, 5, 10. While a weak dependence with Ra is noticed on the drag, a profound effect takes place with the lift. Initially, C_L increases slowly with time. Later, however, the lift not only begins to decrease with increasing Ra; it also becomes negative. The plots suggest, though, that this is a temporary stall, as the curves are seen to level out near $t = 3$.

To more thoroughly explore the mixed convection regime as well as to make some predictions into the behaviour of the flow for large times, simulations for the cases $R = 50$, $Ra = 10$ and $R = 50$, $Ra = 0$ were performed and contrasted for times up to $t = 10$. Selected streamline and isotherm snapshots are illustrated in Figs. 16a–e and 17a–e respectively for the times $t = 3$, 4, 6, 7, 10 for the case $R = 50$, $Ra = 10$. The accelerating flow, vortex shedding process, and thermal plume evolution are all clearly evident in these plots. When these

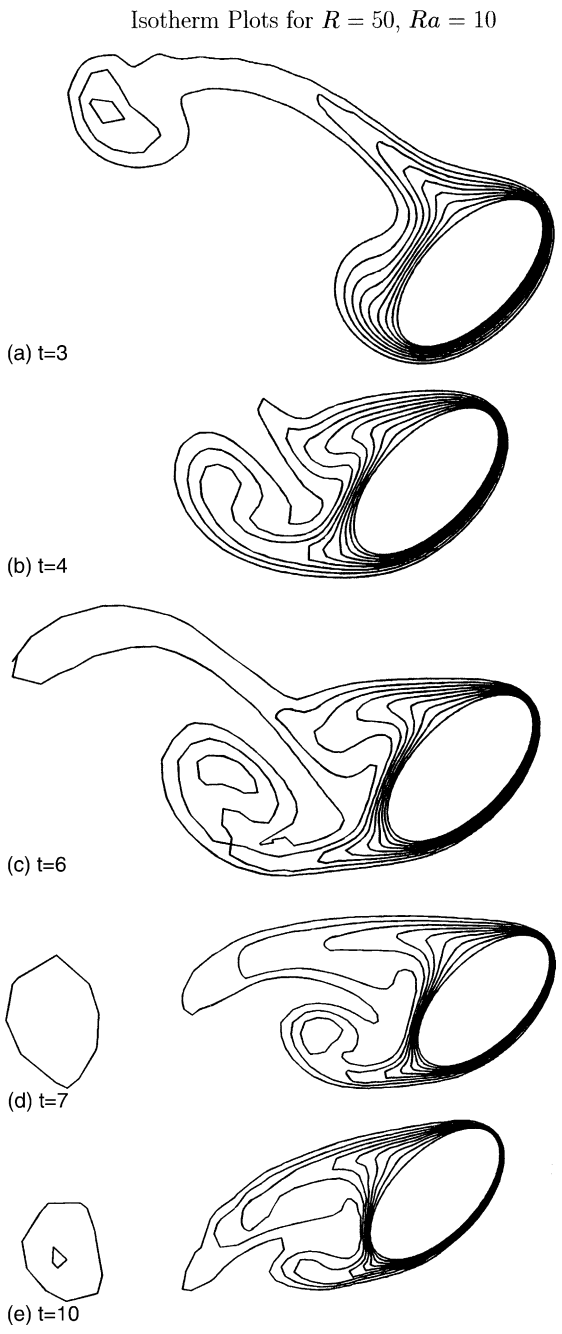

Fig. 17. Isotherm plots for $R = 50$, $Ra = 10$ at times: (a) $t = 3$, (b) $t = 4$, (c) $t = 6$, (d) $t = 7$ and (e) $t = 10$.

plots were compared with the corresponding ones for the forced convection case $Ra = 0$ and $R = 50$, it becomes apparent that as time increases the flow patterns become more and more similar. This is not the case during the early stages of the flow though. Based on these comparisons we can make some intuitive extra-

polations into the flow behaviour for large times. We expect that advection will eventually dominate over buoyancy as time advances due to the accelerating nature of the flow. Thus, the effect of buoyancy will have the greatest impact on the flow during the initial stages when the flow velocities are relatively small. For larger times the flow appears to approach that of forced convection. We suspect that this eventual behaviour will occur regardless of the values of R and Ra; the only difference will be in the time taken to approach the limit of forced convection.

6. Conclusions

Reported in this paper was the start-up thermal-fluid problem associated with a stationary isothermal inclined elliptic cylinder placed in a uniformly accelerating viscous incompressible Boussinesq fluid. Two forms of solution were presented: an approximate analytical series solution expressed in powers of t and λ as well as a numerical technique involving both finite difference and spectral methods. Both solutions were found to be in good agreement for small times and moderately large Reynolds numbers.

This work attempts to highlight the importance of the analytical solution. Here, it provided invaluable information regarding the early flow and heat transfer process. Not only was it used to verify that the numerical scheme was running correctly, more importantly it furnished actual formulae for practical quantities such as the drag, lift and Nusselt number. For instances where the initial conditions are not well behaved, such as cases when the body is started impulsively from rest, the analytical solution can be used to generate an initial condition at a time slightly past the impulsive start when the solution becomes well behaved. In addition it provided information regarding the values of some of the computational parameters such as the number of terms required in the truncated Fourier series as well as the location of the outer boundary. This helps to reduce the number of computational runs which would otherwise be necessary in order to determine these values empirically. Lastly, since the geometry considered is flexible, the analytical solution applies to all elliptical cross sections and by taking appropriate limits it may even apply to the special cases of a flat plate and circular cylinder. We note, though, that there are unanswered questions surrounding the series solution found. For example, what is the interval of convergence of the solution with respect to the parameters t and λ?

Some interesting phenomena during the initial stages of the flow have been reported owing to the buoyancy force. One important observation is that increasing Ra has the effect of delaying the vortex shedding process. In addition, increasing Ra enhances the formation of a thermal plume near the leading tip which grows larger in extent than the thermal wake formed behind the trailing tip. Most notably, the lift coefficient is significantly dependent on Ra; at later times it begins to decrease and becomes negative. However, this trend is not expected to last. For larger times, though, the flow is expected to resemble that of forced convection due to the steady increase in the velocity field.

Acknowledgements

Financial support for this research was provided by the Natural Sciences and Engineering Research Council of Canada. We also acknowledge Mr. Scott Gusba for proving the result (37) of this paper.

Appendix A. Derivation of drag and lift coefficients

Outlined below is a brief derivation of the drag and lift coefficients C_D and C_L respectively. The unsteady dimensional momentum equations for a viscous incompressible fluid expressed in primitive variables can be written in vector form as

$$\frac{\partial \vec{V}}{\partial t} - (\vec{V} \times \vec{W}) = -\nabla\left(\frac{P}{\rho_0} + \frac{1}{2}\vec{V}\cdot\vec{V}\right) - \nu\nabla \times \vec{W} + \left(\frac{\rho}{\rho_0}\right)\vec{g}, \tag{A.1}$$

where $\vec{g} = -g(\sin\eta, \cos\eta, 0)$ and $\rho/\rho_0 = 1 - \alpha(T - T_\infty)$. Here, $\vec{V} = (u, v, 0)$ is the velocity in the accelerating frame of reference, $\vec{W} = \nabla \times \vec{V} = (0, 0, \zeta)$ and P denotes the pressure. In dimensionless form the above can be rewritten as

$$\frac{\partial \vec{V}}{\partial t} - (\vec{V} \times \vec{W}) = -\nabla\left(P^* + \frac{1}{2}\vec{V}\cdot\vec{V}\right) - \frac{2}{R}\nabla \times \vec{W} + Ra\phi(\sin\eta, \cos\eta, 0), \tag{A.2}$$

where $P^* = P/\rho_0 + G$ with G denoting the potential satisfying $\nabla G = -\vec{g}/b - (1, 0, 0)$, in which $(1, 0, 0)$ is the dimensionless translational acceleration of the cylinder. The θ-component of the above equation becomes

$$\frac{\partial v_\theta}{\partial t} + v_\xi\zeta = -\frac{1}{M}\frac{\partial}{\partial\theta}\left(P^* + \frac{1}{2}[v_\xi^2 + v_\theta^2]\right) + \frac{2}{RM}\frac{\partial\zeta}{\partial\xi} + \frac{1}{M}Ra\phi(\sinh(\xi + \xi_0)\cos\eta\cos\theta - \cosh(\xi + \xi_0)\sin\eta\sin\theta). \tag{A.3}$$

On the cylinder surface (A.3) simplifies greatly owing to the impermeability, no-slip and isothermal conditions, $v_\xi = v_\theta = 0$ and $\phi = 1$, and becomes

$$\left(\frac{\partial P^*}{\partial \theta}\right)_{\xi=0} = \frac{2}{R}\left(\frac{\partial \zeta}{\partial \xi}\right)_{\xi=0} + Ra(\sinh\xi_0 \cos\eta\cos\theta - \cosh\xi_0 \sin\eta\sin\theta). \quad (A.4)$$

The forces in the x and y directions, X and Y respectively, can be obtained by integrating the pressure and frictional stresses on the surface as follows:

$$X = -\oint_C P_0^* \,\mathrm{d}y + \frac{2}{R}\oint_C \zeta_0 \,\mathrm{d}x,$$

$$Y = \oint_C P_0^* \,\mathrm{d}x + \frac{2}{R}\oint_C \zeta_0 \,\mathrm{d}y.$$

Making use of (A.4) and simplifying then leads to Eqs. (76) and (77).

References

[1] W.M. Collins, S.C.R. Dennis, Symmetrical flow past a uniformly accelerated circular cylinder, J. Fluid Mech. 65 (1974) 461–480.

[2] H.M. Badr, S.C.R. Dennis, S. Kocabiyik, Symmetrical flow past an accelerated circular cylinder, J. Fluid Mech. 308 (1996) 97–110.

[3] S.J.D. D'Alessio, F.W. Chapman, The initial flow past a uniformly accelerating inclined elliptic cylinder, Can. Appl. Math. Q 8 (2000) 215–245.

[4] V.A. Patel, Flow around the impulsively started elliptic cylinder at various angles of attack, Comput. Fluids 9 (1981) 435–462.

[5] K. Shintani, A. Umemura, A. Takano, Low Reynolds number flow past an elliptic cylinder, J. Fluid Mech. 136 (1983) 227–289.

[6] S.J.D. D'Alessio, Steady, unsteady and linear stability of flow past an elliptic cylinder, Can. Appl. Math. Q 4 (1996) 341–379.

[7] M.T. Nair, T.K. Sengupta, Unsteady flow past elliptic cylinders, J. Fluids Struct. 11 (1997) 555–595.

[8] H.M. Badr, S.C.R. Dennis, S. Kocabiyik, Numerical simulation of the unsteady flow over an elliptic cylinder at different orientations, Int. J. Numer. Meth. Fluids 37 (2001) 905–931.

[9] H.M. Badr, Laminar combined convection from a horizontal cylinder, parallel and contra flow regimes, Int. J. Heat Mass Transfer 27 (1984) 15–27.

[10] A. Bassam, K. Abu-Hijleh, Laminar mixed convection correlations for an isothermal cylinder in cross flow at different angles of attack, Int. J. Heat Mass Transfer 42 (1999) 1383–1388.

[11] A. Bassam, K. Abu-Hijleh, Entropy generation in laminar convection from an isothermal cylinder in cross flow, Energy 23 (1998) 851–857.

[12] H.M. Badr, F.M. Mahfouz, Mixed convection from a cylinder oscillating vertically in a quiescent fluid, Heat Mass Transfer 38 (2002) 477–486.

[13] S. Nguyen, H. Paik, R. Douglas, Unsteady mixed convection about a rotating circular cylinder with small fluctuations in the free-stream velocity, Int. J. Heat Mass Transfer 36 (1995) 3311–3325.

[14] E.H. Ahmad, H.M. Badr, Mixed convection from an elliptic tube placed in a fluctuating free stream, Int. J. Sci. 39 (2001) 669–693.

[15] H. Nishiyama, T. Ota, T. Matsuno, Heat transfer and flow around elliptic cylinders in a tandem arrangement, JSME Int. J. Ser. II 31 (1988) 410–419.

[16] S.C.R. Dennis, L. Quartapelle, Some uses of Green's theorem in solving the Navier–Stokes equations, Int. J. Numer. Meth. Fluids 9 (1989) 871–890.

[17] A.N. Staniforth, Studies of symmetrical and asymmetrical viscous flows past impulsively started cylinders, Ph.D. thesis, University of Western Ontario, London, Canada, 1973.

[18] H.M. Badr, S.C.R. Dennis, Time-dependent viscous flow past an impulsively started rotating and translating circular cylinder, J. Fluid Mech. 158 (1985) 447–488.

[19] S.J.D. D'Alessio, S.C.R. Dennis, P. Nguyen, Unsteady viscous flow past an impulsively started oscillating and translating elliptic cylinder, J. Eng. Math. 35 (1999) 339–357.

[20] S.J.D. D'Alessio, S. Kocabiyik, Numerical simulation of the flow induced by a transversely oscillating inclined elliptic cylinder, J. Fluids Struct. 15 (2001) 691–715.

[21] M.G. Saunders, Initial stages of mixed convective heat transfer past an accelerating inclined elliptic cylinder, M. Math. thesis, University of Waterloo, Waterloo, Canada, 2002.

[22] S.C.R. Dennis, Gau-Zu Chang, Numerical integration of the Navier–Stokes equations in two dimensions, Technical Summary Report No. 859, Mathematics Research Center, University of Wisconsin, 1969.

[23] L.N.G. Filon, On a quadrature formula for trigonometric integrals, Proc. Roy. Soc. Edinburgh (1929) 38–47.